Journal of Materials Chemistry A

ROYAL SOCIETY OF CHEMISTRY

PAPER

View Article Online
View Journal | View Issue

Cite this: J. Mater. Chem. A, 2020, 8, 7235

The critical role of configurational flexibility in facilitating reversible reactive metal deposition from borohydride solutions†

Nathan T. Hahn, [ab] Julian Self, [acd] Trevor J. Seguin,[ac] Darren M. Driscoll, [ae] Mark A. Rodriguez,[b] Mahalingam Balasubramanian, [ae] Kristin A. Persson [acd] and Kevin R. Zavadil *[ab]

Received 3rd March 2020
Accepted 22nd March 2020

DOI: 10.1039/d0ta02502j

rsc.li/materials-a

Development of calcium metal batteries has been historically frustrated by a lack of electrolytes capable of supporting reversible calcium electrodeposition. In this paper, we report the study of an electrolyte consisting of $Ca(BH_4)_2$ in tetrahydrofuran (THF) to gain important insight into the role of the liquid solvation environment in facilitating the reversible electrodeposition of this highly reactive, divalent metal. Through interrogation of the Ca^{2+} solvation environment and comparison with Mg^{2+} analogs, we show that an ability to reversibly electrodeposit metal at reasonable rates is strongly regulated by dication charge density and polarizability. Our results indicate that the greater polarizability of Ca^{2+} over Mg^{2+} confers greater configurational flexibility, enabling ionic cluster formation *via* neutral multimer intermediates. Increased concentration of the proposed electroactive species, $CaBH_4^+$, enables rapid and stable delivery of Ca^{2+} to the electrode interface. This work helps set the stage for future progress in the development of electrolytes for calcium and other divalent metal batteries.

Introduction

Batteries based on alkaline earth metals (Mg, Ca) have been proposed as potential "beyond Li-ion" electrochemical energy storage concepts.[1] The large volumetric and gravimetric capacity gains afforded by the use of an active metal anode as opposed to an insertion anode (*e.g.* LiC_6) are responsible for much of this promise. However, unlike the Li-ion case, reactivity of divalent metals with liquid electrolytes does not yield protective, cation conductive interfacial films required for efficient metal cycling. Mg has enjoyed significant research interest owing to its more modest cathodic standard potential *vs.* SHE (−2.36 V for Mg *vs.* −2.87 V for Ca), reducing the probability of parasitic electrolyte reduction and electrode passivation.[2] While many novel electrolytes have been developed for reversible Mg plating over the past several years,[3–7] progress on Ca has been slower, punctuated by a recent demonstration of surface-film mediated, quasi-reversible Ca plating at high temperature and low coulombic efficiency (CE).[8] Despite limited progress, development in the area of Ca^{2+}-insertion cathodes has continued undaunted, awaiting a breakthrough in Ca plating electrolytes to enable rechargeable calcium batteries.[9,10] Such a breakthrough came recently, as work by Wang *et al.* demonstrated the possibility of reversible Ca electrodeposition at room temperature in an organic $Ca(BH_4)_2$/tetrahydrofuran (THF) electrolyte at an encouragingly high CE (~95%) despite apparent formation of a CaH_2 byproduct through THF dehydrogenation.[11] More recently, Li *et al.* and Shyamsunder *et al.* have demonstrated reversible, room temperature Ca electrodeposition in the absence of both the strong reducing borohydride anion and the production of CaH_2, (using calcium tetrakis(hexafluoroisopropyloxy) borate in 1,2-dimethoxyethane) albeit at lower coulombic efficiency and as a discontinuous metal deposit containing CaF_2.[12,13] We focus herein on the $Ca(BH_4)_2$/THF electrolyte as an important benchmark system that is differentiated by its potential for richer coordination chemistry as determined by the strongly complexing BH_4^- anion.[14–16] Furthermore, the connection between this electrolyte's surprising functionality and the uniqueness of its solvation environment has not been fully explored. Recently published work by Ta *et al.* offered an additional perspective regarding electrolyte decomposition, citing evidence of BH_4^- conversion to BH_3 during cycling apparently resulting from hydride transfer to the substrate surface.[17] The differing explanations of electrolyte function offered by Wang *et al.* and Ta

[a]Joint Center for Energy Storage Research, Lemont, IL 60439, USA
[b]Material, Physical and Chemical Sciences Center, Sandia National Laboratories, Albuquerque, NM 87185, USA. E-mail: krzavad@sandia.gov
[c]Energy Technologies Area, Lawrence Berkeley National Laboratory, Berkeley, CA 94720, USA
[d]Department of Materials Science and Engineering, University of California Berkeley, Berkeley, CA 94720, USA
[e]Advanced Photon Source, Argonne National Laboratory, Lemont, IL 60439, USA

† Electronic supplementary information (ESI) available. CCDC 1964638. For ESI and crystallographic data in CIF or other electronic format see DOI: 10.1039/d0ta02502j

et al. motivate a more detailed study of the role of Ca^{2+} coordination in $Ca(BH_4)_2$/THF electrolyte behavior.

In this paper, we build on these exciting demonstrations of Ca plating by providing a thorough understanding of the Ca^{2+} solvation environment in the $Ca(BH_4)_2$/THF electrolyte system. Through systematic interrogation of the solvation environment using experimental and computational techniques, we reveal unexpected solvation trends in which ion association, mediated by multimeric cluster formation, leads to enhanced delivery of Ca^{2+} to the electrode surface while minimizing parasitic losses at high concentration (see Scheme 1). These attributes are contrasted with those of $Mg(BH_4)_2$ electrolytes, which have been the subject of several recent studies.[5,18–21] Our integrated investigation demonstrates that the relative concentration of ionic clusters is enhanced in high concentration $Ca(BH_4)_2$/THF, and that BH_4^- is strongly coordinated to Ca^{2+} within these clusters. From this analysis, we propose that the electroactive cationic species is $CaBH_4^+$ and that this species is responsible for delivery of Ca^{2+} to the electrode. We further demonstrate that the ability of Ca^{2+} to form a greater variety of coordination structures (*i.e.* configurational flexibility) such as multimeric solvates is critical for forming high concentrations of the $CaBH_4^+$ species. The contrast between Ca^{2+} and Mg^{2+} coordination demonstrated herein links to a more general understanding of cation size and coordination tendencies as observed in biological applications.[22,23] Our findings have important implications for the design of solvation environments for cation delivery under extremely reducing conditions, such as those existing at Mg and Ca metal anodes. As the community grapples with the origins and mechanisms of electrolyte breakdown under these conditions, a clear understanding of the pertinent solvation regimes is needed.

Experimental

Materials and methods

All reagent handling and electrochemical testing was performed in an Ar-filled glove box ($H_2O \leq 1$ ppm, $O_2 \leq 0.1$ ppm). $Ca(BH_4)_2$ and $Ca(BH_4)_2 \cdot 2THF$ (99.4–100.9% BH_4^-), $Mg(BH_4)_2$ (>95%), and $LiBH_4$ (95%) salts were purchased from Sigma-Aldrich and used as received. NBu_4BH_4 (96%) was purchased from TCI chemicals and used as received. Due to their intrinsic reactivity toward water these borohydride salts were not dried further. Hexafluoroisopropanol was purchased from Sigma Aldrich and dried using 3A/4A molecular sieves. Calcium hexafluoroisopropoxyborate ($Ca(BHFIP)_2$) was synthesized by reaction between $Ca(BH_4)_2$ and hexafluoroisopropanol, following a published procedure.[12] THF (anhydrous, 99.9%) was purchased from Sigma-Aldrich, distilled, and stored over 3A/4A molecular sieves and activated alumina prior to use. Karl-Fischer analysis indicated a typical THF water content of less than 15 ppm. Electrolytes with targeted solvent : salt ratios were synthesized by adding both $Ca(BH_4)_2$ and THF by weight and concentrations were calculated by measuring solution densities with volumetric flasks in several cases.

Raman spectroscopy was performed on a WITec Confocal Raman Microscope using a 532 nm excitation laser. Spectral frequencies were calibrated using the Raman peak of a Si wafer (520.4 cm^{-1}). Curve fitting analysis was used to quantify the fraction of THF–Ca^{2+} coordination and qualitatively assess the nature of BH_4^-–Ca^{2+} coordination (ESI Fig. S1†). Energy dispersive X-ray analyses of Ca deposits were conducted on a FEI Helios Nanolab 600 G3 scanning electron microscope.

Electrolyte X-ray absorption spectroscopy (XAS) measurements at the Ca K-edge were performed at the bending magnet beamline at Sector 9 of the Advance Photon Source, Argonne National Laboratory. The liquid electrolytes were deposited into stacks of porous polyolefin discs (Celgard, 25 μm in thickness) and sealed within an aluminized-mylar pouch. The incident beam was monochromatized with a Si(111) monochromator and harmonic suppression was achieved using a X-ray mirror set to a cutoff energy of 6 KeV. Background removal and normalization for extended X-ray absorption fine structure (EXAFS) analysis was performed in the Athena analysis program.[24] The slowly oscillating background component was removed and the raw EXAFS signal, $\chi(k)$, was extracted by using a cut-off distance (R_{bkg}) of 1.3 Å. All $\chi(k)$ data were weighted by $k^1 - k^3$ and Fourier transformed between $3 < k < 11.8$ $Å^{-1}$. A Hanning window function with a $dk = 1$ was employed. Model scattering pathways attributed to Ca–THF (including both single scattering and multiple scattering

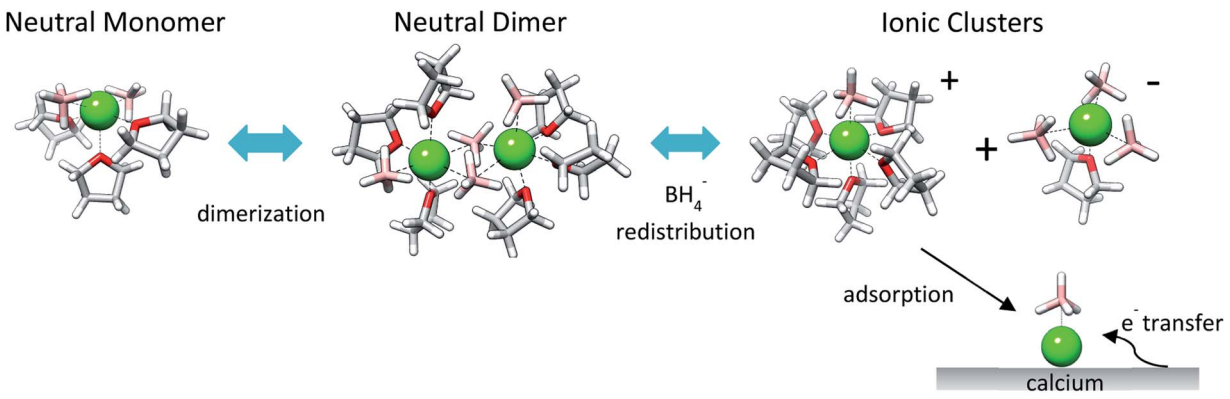

Scheme 1 Reaction pathway for ionic cluster formation in the $THF_nCa(BH_4)_2$ electrolyte system yielding $CaBH_4^+$ as the species responsible for Ca electrodeposition.

pathways), Ca–BH_4 and Ca–Ca dimers were calculated using the *ab initio* code FEFF 6.0 and used to identify the major contributions in the experimental EXAFS data using the ARTEMIS software package.[24,25] Full details of the XAS measurements could be found in the ESI document.†

Crystalline solvates of $Ca(BH_4)_2$ in THF, G1, and G2 were produced for X-ray diffraction (XRD) and Raman spectroscopy by creating saturated solutions at elevated temperature and cooling the solutions slowly to room temperature. Single crystal XRD was performed using a Bruker D8 Venture dual-source single crystal diffractometer employing Mo Ka radiation (0.07107 nm) and Cu Ka radiation (0.154060 nm) with samples at room temperature under a flowing stream of N_2. Solvate crystals were transferred from the glove box and analyzed while immersed in Fluorolube oil to minimize exposure to water vapor. Structure determination for the single crystal samples was performed using the Apex III (v2017.3-0) software as described in the ESI document.†

Electrochemical experiments were performed in a sealed, small volume, three-electrode cell with freshly abraded Ca or Mg rods (99.5%, ESPI Metals, abraded just prior to immersion) as reference and counter electrodes using a Solartron Modulab potentiostat. The reference potential of the M/M^{2+} couples were very stable across multiple electrolyte versions and as a function of time as determined by repeated metal deposition/stripping cyclic voltammograms (CV). Working electrodes consisted of mirror-polished Au (0.02 cm^2) disks set in CTFE sleeves (BASi). Ionic conductivity was measured with impedance spectroscopy using a custom-built probe consisting of parallel Pt electrodes. The cell constant of this conductivity probe was calibrated repeatedly with multiple concentrations of aqueous KCl solution. Molar equivalent conductivity values were obtained by dividing the measured conductivity by the salt concentration.

Hazards: Borohydride compounds are reducing agents which react strongly with oxidizers and acids, including water. This trait, combined with the high volatility and flammability of THF means that great care should be taken in the handling and disposal of the solutions discussed in this work, including avoiding their exposure to air and working with minimal quantities.

Computational methods

Molecular dynamics (MD) simulations were carried out with the GROMACS software,[26] and initial configurations were prepared using Packmol.[27] Forcefield parameters for THF were taken from Spoel *et al.*,[28] Ca^{2+} parameters from the standard OPLS library, and BH_4^- parameters from Rajput *et al.*[29–31] The methodology used to calculate permittivity change from individual salt species follows Self *et al.*[32] Further details of the MD simulations can be found in the ESI document.† Quantum chemistry calculations were undertaken with Gaussian 16 software.[33] The M06 functional was employed with the 6-311g(d,p) Pople basis set for geometry optimizations,[34] and single point energies were then obtained using the optimized geometries with the Def2-TZVPPD basis set to obtain final free energies.[35] Further details of the quantum chemistry calculations can be found in the ESI document.†

Results and discussion

Formation of electroactive $CaBH_4^+$

The critical role of Ca–BH_4 coordination in defining the electrochemical activity of the $Ca(BH_4)_2$/THF electrolyte is indicated by the strong correlation between Ca deposition rate/efficiency and salt concentration, as demonstrated by CV (Fig. 1a). The fact that metallic Ca is being deposited is confirmed through energy dispersive X-ray analysis in a scanning electron microscope (ESI Fig. S2†) Representative CE values measured by CV increase from 65% at 0.43 M to 97% at 1.65 M. The maximal efficiency values measured at high concentration are similar to previously reported values.[11,17] The maximum deposition current densities reached at −0.8 V under these conditions also increase significantly from 0.57 mA cm^{-2} at 0.43 M to 12.9 mA cm^{-2} at 1.65 M. Since these potentiodynamic CE measurements could be influenced by the large differences in plating and stripping rates and capacities achieved at different concentrations, we conducted constant current chronopotentiometric CE measurements at fixed capacity on Au working electrodes across this same concentration series. Example chronopotentiograms (CP), with time expressed as cumulative areal capacity, are shown in Fig. 1b and indicate that for a given current density (in this case 0.5 mA cm^{-2}), electrode polarization increases significantly at low salt concentrations. Complete sets of CP traces at various current densities for all three concentrations are shown in the ESI, Fig. S3.† Both the CV and CP deposition traces indicate low nucleation overpotentials for Ca on Au (*e.g.*, 170 mV at 1.65 M). A previous report proposed that adsorbed hydride species can facilitate Ca nucleation on Au, making it a better substrate for high efficiency Ca deposition than Pt.[17] Inspection of our low current dissolution traces indicates surface alloying/de-alloying between Ca and Au occurs, possibly enhancing the nucleation density of Ca on Au, thereby activating (as opposed to depassivating) the surface for Ca deposition. Evidence for alloying is clearly observed in Fig. 1b during dissolution where a small anodic shift in the dissolution potential signals a transition from bulk Ca stripping to de-alloying (52 to 170 mV at 1.65 M). Further investigation of this phenomenon is beyond the scope of this work and will be the subject of a future report.

Coulombic efficiency remains a strong function of salt concentration under conditions of constant deposition rate and capacity, as shown in Fig. 1c For example, at a modest current density of 0.5 mA cm^{-2} the CE values increase from 73% at 0.43 M to 92% at 1.65 M. Higher steady-state current densities (4 mA cm^{-2}), which are readily supported with acceptable overpotentials at high $Ca(BH_4)_2$ concentrations, enable further increases in CE up to a maximum value of > 97%, consistent with the aforementioned potentiodynamic values. The observed dependence of CE on current density regardless of concentration probably relates to changes in the relative rates of Ca^{2+} deposition and electrolyte reaction; the faster Ca^{2+} is plated and stripped, the less time is available for reaction between electrolyte constituents and fresh calcium metal.[11] These trends highlight the importance of an electrolyte's ability to transport and deliver Ca^{2+} at high

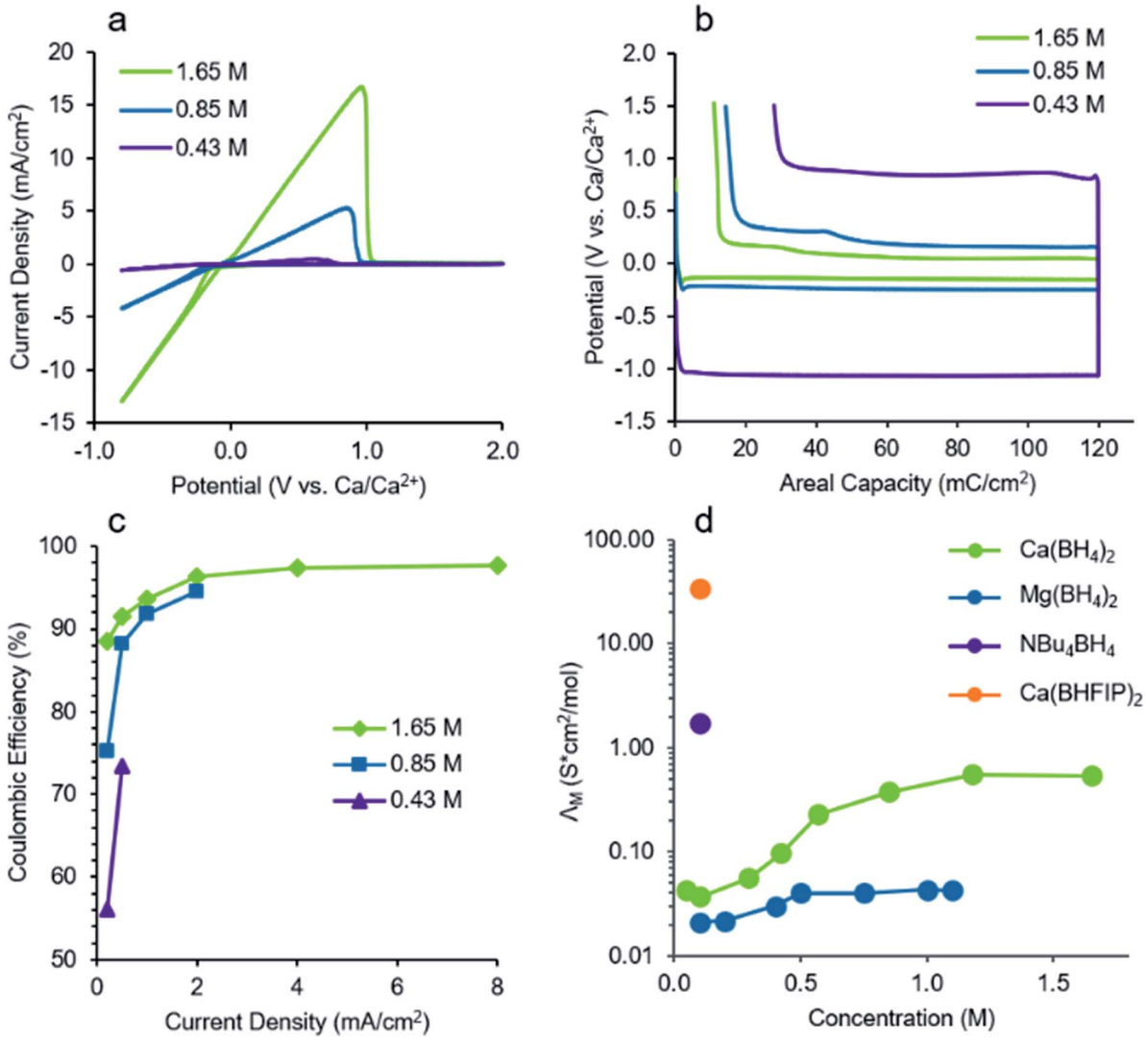

Fig. 1 (a) Cyclic voltammograms (scan rate = 50 mV s^{-1}) of calcium electrodeposition and stripping in $Ca(BH_4)_2$/THF on Au as a function of salt concentration (3rd cycle). (b) Chronopotentiograms measured for galvanostatic deposition and stripping of calcium on Au (1st cycle) as a function of $Ca(BH_4)_2$ concentration in THF at 0.5 mA cm^{-2}. (c) Average CE values measured during galvanostatic Ca plating/stripping at a Au electrode as a function of current density and $Ca(BH_4)_2$ concentration in THF. Deposition capacity was kept constant at 120 mC cm^{-2} or ~160 nm of Ca, similar to the amount deposited during a CV cycle. (d) Molar ionic conductivities measured for select salts in THF as a function of concentration.

rates in order to spare parasitic losses, which may be driven by reaction of THF and/or BH_4^- with the highly reactive metallic Ca deposit or the cathodically polarized substrate.[11,17] Despite the fact that 0.43 M represents a concentration well within the range of typical high-performing aprotic Mg-salt electrolytes,[3,36–38] the electrochemical rate and reversibility of $Ca(BH_4)_2$/THF at this concentration are far inferior to those observed at higher concentration ranges, reflecting the importance of associated Ca–BH_4 clusters in facilitating Ca^{2+} delivery.

Ionic cluster formation for $Ca(BH_4)_2$ in THF is clearly demonstrated by molar equivalent ionic conductivity (Λ_M) measurements, which reveal an increase in relative ionic populations as a function of salt concentration (Fig. 1d). This relationship between ionicity and concentration, though unlike that of traditional aqueous electrolytes, has previously been observed for electrolytes consisting of low permittivity solvents.[39–43] The strong association tendencies of BH_4^- with metal cations in THF, as found in previous studies,[18–20] suggests that $Ca(BH_4)_2$ would be likewise strongly associating in THF even at low concentrations. Indeed, the very low ionic conductivity measured at 0.1 M (0.0038 mS cm^{-1}) implies the dominance of undissociated neutral species at this concentration since this conductivity value is nearly two orders of magnitude lower than the value we measure (0.17 mS cm^{-1}) for a more weakly-associating tetrabutylammonium (NBu_4^+) borohydride solution at the same concentration in THF. When $Ca(BH_4)_2$ is substituted by the still more weakly coordinated $Ca(BHFIP)_2$ salt,[12,13] ionic conductivity increases by yet another order of magnitude to 3.4 mS cm^{-1}. The magnitude of these conductivity differences unambiguously demonstrates the strong coordination of BH_4^- to Ca^{2+} in THF. Interestingly, Λ_M values measured in analogous $Mg(BH_4)_2$ solutions are even lower than

those of $Ca(BH_4)_2$ and increase more modestly with increasing concentration, indicating that ionic cluster formation is further inhibited by the presence of the higher charge density Mg^{2+} cation (Fig. 1d). This inhibition of ionic cluster formation is also manifested in a lower Mg deposition rate and CE (74%) that we measure for saturated $Mg(BH_4)_2$/THF (~1.1 M) arguing that the dominance of neutral clusters is the primary performance-limiting factor (ESI, Fig. S4†). While the influence of interfacial factors cannot be ruled out, the stark difference in ion populations points to the solvation environment as a primary differentiating element between $Ca(BH_4)_2$ and $Mg(BH_4)_2$. Indeed, both experimental and theoretical studies have shown that alkali borohydride additives such as $LiBH_4$ are required to facilitate conversion of neutral $Mg(BH_4)_2$ clusters to associated ionic clusters, *e.g.* $MgBH_4^+$, and thus attain acceptable ionic conductivity and electrochemical behavior.[5,18,19] In contrast, the larger and more polarizable Ca^{2+} cation clearly provides a route to ionic clusters even in the absence of borohydride additives.

The likely structures of the dominant ionic calcium species are provided by DFT cluster free energy optimization. In these calculations the free energies of formation of explicitly solvated and structurally optimized ionic clusters residing within the THF dielectric medium ($\varepsilon_{THF} = 7.4$) were compared with those of a stoichiometric number of neutral cluster "reactants" to compute a net free energy change for each ion formation "reaction" (Fig. 2). The dependence of these free energies on THF coordination number is shown in the ESI, Fig. S5.† Immediately apparent from these calculations is the unlikelihood of the formation of fully dissociated Ca^{2+} and BH_4^- species ($\Delta G > 1$ eV!), a finding which is consistent with calculations reported for $Mg(BH_4)_2$/THF.[18,19,31] In fact, all ionic clusters in this system possess a significant equilibrium free energy of ~0.4 eV or higher. These endergonic values would predict small ion populations of less than 1 mM based on a simple equilibrium relationship ($K = e^{(-\Delta G/kT)}$), although actual ion populations must be larger at high salt concentrations given the measured conductivity trend. The calculations identify $CaBH_4^+$ as the primary cation in solution and $Ca(BH_4)_3^-$ as the primary anion, based on comparison with the other calculated structures. Stabilization of these ionic Ca^{2+} clusters by coordinating BH_4^- is clearly a requirement in this electrolyte, which arises from a lowering of the effective charge density of the ionic cluster. Hence, we propose that $CaBH_4^+$ is the primary "electroactive" species enabling high rate Ca deposition in $Ca(BH_4)_2$/THF.

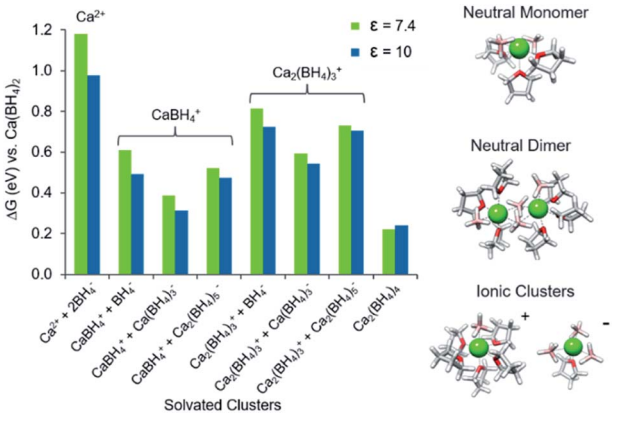

Fig. 2 Computed free energy changes for the formation of several proposed combinations of solution species from solvated $Ca(BH_4)_2$ in THF. Calculations were performed assuming both explicit solvation and a dielectric medium with strength equal either to the intrinsic permittivity of THF (7.4) or to an elevated solution permittivity value (10) that could arise from a high concentration of dipolar ion pairs ($CaBH_4^+$). The ionic couples are grouped by cationic species to emphasize the relative favorability of $CaBH_4^+$. Key structural examples are shown at right.

We note that although the above results indicate that $CaBH_4^+$ and $Ca(BH_4)_3^-$ are the most energetically favored of the ionic species, we did not consider aggregates larger than $Ca_2(BH_4)_5^-$. Furthermore, concentration effects and non-idealities (*e.g.* long-range electrostatics), may affect the various cluster equilibria differently, which we plan to investigate in upcoming work. To test whether the presence of dipolar clusters could facilitate formation of ionic species at high concentration through permittivity increases, as previously observed in other strongly associating electrolytes,[32,40,41,44–46] we conducted simulations to determine the influence of several proposed clusters on the solution dielectric constant (ESI, Fig. S6†). The computed lowest free energy electrolyte structure, $THF_3Ca(BH_4)_2$, possesses a bent geometry and a calculated dipole moment of 5 Debye. However, solvation of this cluster requires three THF molecules, which reduces the free solvent contribution to solution permittivity. Therefore, the net effect of dissolving $Ca(BH_4)_2$ to form neutral monomers should be reduction in solution permittivity. In contrast, the contact ion pair (CIP) cation $THF_5CaBH_4^+$, the minimum energy cationic cluster, possesses a stronger dipole moment that overcomes the effects of free solvent loss, and other possible clusters such as solvent shared ion pairs (SIP) could theoretically contribute even more dramatically. To estimate the potential impact of a solution permittivity increase on ion formation energetics, we recalculated the free energy values for the various ionic species assuming a dielectric constant of 10.0, representing a solution containing a concentration of 0.35 M $CaBH_4^+$ clusters (Fig. 2). The resulting free energies for forming ionic species are all reduced, reflecting stabilization *via* reduced interionic electrostatic interactions. Hence, a permittivity increase due to the creation of $CaBH_4^+$ could theoretically drive increased ionicity with concentration as we observe for $Ca(BH_4)_2$/THF, and further studies utilizing dielectric relaxation spectroscopy to determine the true magnitude of the permittivity changes in these solutions as a function of concentration are planned. Another possible explanation for the increase in molar conductivity could be the lowering of activity coefficients of the ionic clusters at higher ionic strengths from long-range electrostatics, as predicted by Debye–Huckel theory.[47]

Regardless of the true magnitude of these permittivity effects, the free energy calculations presented here argue for a solution dominated by ion association, resulting in coordination of all Ca^{2+} cations to at least one BH_4^- anion. Therefore, we can confidently state that the active species responsible for ion transport and calcium metal plating contains coordinated

BH_4^-. The free energy trends indicate that the most stable and therefore most prevalent ionic species of this kind in solution is $CaBH_4^+$, which is formed along with $Ca(BH_4)_3^-$ from the redistribution of BH_4^- anions between $Ca(BH_4)_2$ clusters. CIP cations of this type have previously been invoked as an important intermediate in chloride-based Mg^{2+} electrolytes, where $MgCl^+$ species participate in both the Mg deposition and cathode insertion mechanisms.[48–52] Therefore, its presence within a high-functioning Ca^{2+} electrolyte represents a critical link between these two alkaline earth metals and provides additional insight into the likely Ca deposition mechanism. From analogy with proposed $MgCl^+$ deposition mechanisms, we propose that Ca deposition generally takes place according to:

$$M(\text{substrate}) + THF_nCaBH_4^+ \rightarrow M\cdots CaBH_4^+(\text{ads}) + n\text{THF} \quad (1)$$

$$M\cdots CaBH_4^+(\text{ads}) + 2e^- \rightarrow M\cdots Ca^0 + BH_4^- \quad (2)$$

Based on this general mechanism of $CaBH_4^+$ desolvation (1) and electronation (2), the ability to form $CaBH_4^+$ becomes a paramount requirement for electrochemical activity of the $Ca(BH_4)_2$/THF electrolyte. We ascribe the significantly reduced ionic conductivity and metal deposition rate of $Mg(BH_4)_2$/THF to difficulty in forming the analogous $MgBH_4^+$ species, as noted by previous researchers.[5,53] In the Mg^{2+} version, it has been proposed that $MgBH_4^+$ forms from liberation of free BH_4^-, a process that our calculations show is unfavorable for $Ca(BH_4)_2$/THF. These observations suggest that the $Ca(BH_4)_2$ electrolyte possesses an alternative, more favorable pathway for creation of the $CaBH_4^+$ species, and our data show that this pathway is enhanced at high salt concentrations. We hypothesize that such a pathway should involve direct interaction between neutral $Ca(BH_4)_2$ clusters to facilitate redistribution of BH_4^- and thus may take place *via* a multimeric intermediate. DFT analysis indicates that $Ca_2(BH_4)_4$ dimers, for example, are even more energetically favorable than the most prevalent ionic species. Hence, a tendency of $Ca(BH_4)_2$ to form multimeric species in THF, as facilitated by the greater configurational flexibility of Ca^{2+} relative to Mg^{2+}, could explain its differing behavior with respect to $Mg(BH_4)_2$ and we further test this hypothesis in the subsequent section.

Ca^{2+} multimers and configurational flexibility

To directly test for the presence of $Ca_n(BH_4)_{2n}\cdot$THF multimers, we performed extended X-ray absorption fine structure (EXAFS) analysis at the Ca K-edge to probe the average coordination structure of Ca^{2+} in a concentrated (1.5 M) $Ca(BH_4)_2$/THF solution. Qualitatively, the EXAFS spectrum of $Ca(BH_4)_2$/THF (shown in both *k*-space and *r*-space with k^1-weighting in Fig. 3a

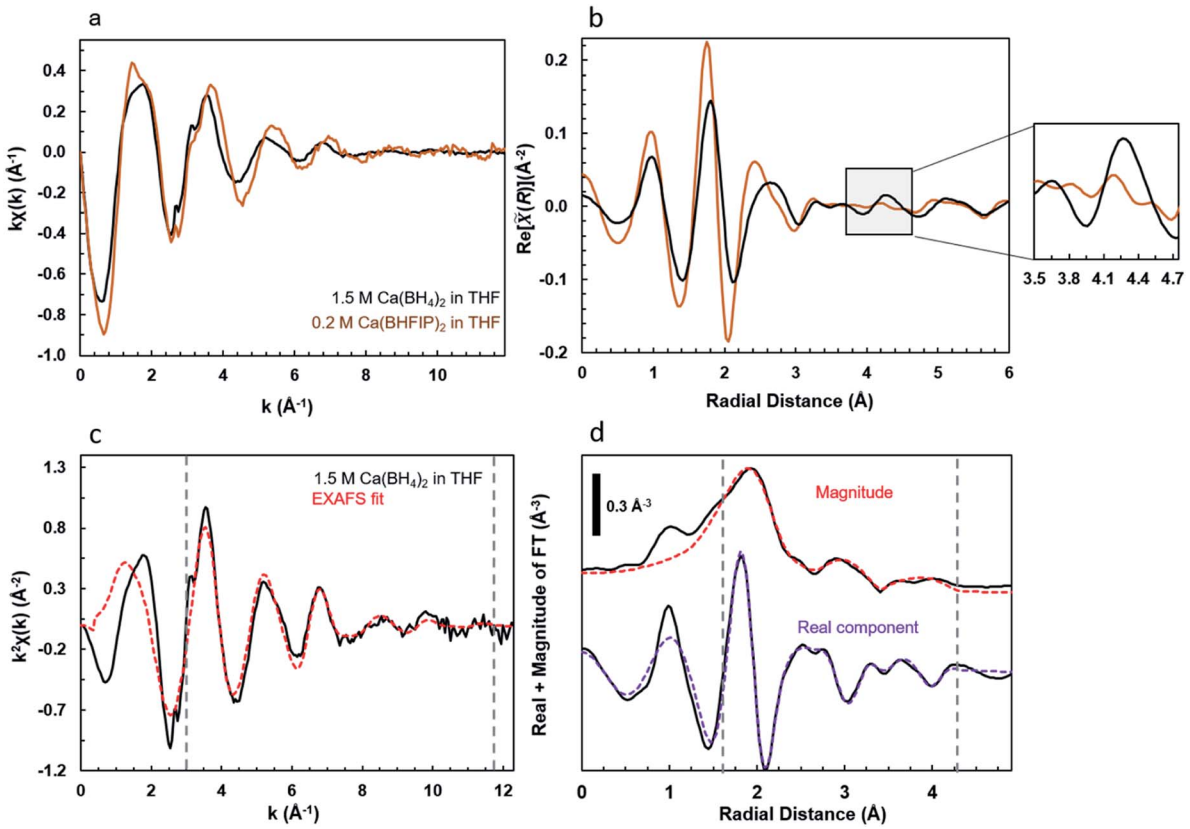

Fig. 3 EXAFS spectral analysis of Ca^{2+} salts in THF. A comparison of the k^1-weighted $\chi(k)$ (panel a) and Re[$\tilde{X}(R)$] spectra (panel b) for the Ca K-edge of 1.5 M $Ca(BH_4)_2$ (black trace) and 0.2 M $Ca(BHFIP)_2$ (orange trace) in THF. Quantitative analysis through EXAFS fitting of *k*-space (panel c) and *r*-space (panel d) for the 1.5 M $Ca(BH_4)_2$/THF system. Spectra are plotted as k^2-weighted. The black traces represent the experimental data and the dashed traces (shown in red and purple) represent the calculated EXAFS fits. Dashed vertical lines represent the respective *k*-window and *r*-window for FT analysis and EXAFS fitting.

and b) shows remarkable differences in both amplitude and phase compared with that of a dilute solution of the strongly dissociating $Ca(BHFIP)_2$ salt in THF. Evidence for the latter's strong dissociation in THF is provided by the aforementioned ionic conductivity measurements (*vide supra*), and therefore we consider this solution to represent a control case in which Ca^{2+} is exclusively coordinated by THF. The *k*-space data illustrate an overall reduction in amplitude and a progressively larger phase shift for the $Ca(BH_4)_2$/THF spectral oscillations with increased *k*. These differences are attributed to changes in oxygen coordination around the Ca^{2+} ion and the introduction of Ca–BH_4 coordination, as predicted by DFT calculations. The clear difference between the two electrolyte solutions is also evident in the corresponding Fourier transform (uncorrected for photoelectron phase shifts); the real component of which is displayed in Fig. 3b. Specifically, a distinct feature (Fig. 3b, inset) is identified in the $Ca(BH_4)_2$ electrolyte at around 4 Å that is absent from the $Ca(BHFIP)_2$ data. This region is of similar radial distance to where DFT optimized geometries predict the presence of a Ca–Ca dimer correlation (ESI, Fig. S7†). These concerted spectral changes, at radial distances consistent with DFT, are strong evidence for the presence of multimers in the concentrated $Ca(BH_4)_2$ solution.

A full quantitative analysis, details of which are provided in the ESI,† confirms the presence of multimers and Ca–BH_4 coordination in high concentration $Ca(BH_4)_2$/THF, as indicated by Ca–Ca and Ca–B correlations in the EXAFS (see ESI, Fig. S8 and S9† for individual contributions). The EXAFS, shown in *k*-space and *r*-space in Fig. 3c and d (k^2-weighting), was fit using the DFT optimized structures as initial models. Excellent agreement was attained between the fitted structural model and the measured EXAFS data when Ca–O_{THF}, Ca–C_{THF}, Ca–BH_4 and Ca–Ca interactions were included in the fit. A full list of parameters and their associated values attained after fitting can be found in the ESI, Table S1.† Noteworthy, is the presence of a Ca–Ca interaction at a distance of 4.44 ± 0.05 Å. Inclusion of this contribution was deemed essential as it statistically improves the fits by almost 50% (ESI, Table S2†). Other potential scattering paths, including the double bounce path from the Ca–O_{THF} correlation around 4.5 Å, were tested and were not found to match the experimental data with the same statistical accuracy. Furthermore, the interaction distances obtained from the EXAFS ensemble structural model are consistent with those determined for DFT-optimized dimer clusters which contain shared BH_4^- anions. The CN values derived from the EXAFS model contain significant uncertainty due to assumptions made regarding the total coordination of Ca^{2+}, as required to minimize the number of independent variables in relation to the information content contained within the EXAFS. However, physically reasonable values of the Debye Waller factors were achieved only when the EXAFS spectrum was fit assuming a total coordination between 7 and 8, suggesting that the THF coordination numbers found in the DFT optimized structures are somewhat underestimated (ESI, Fig. S4†). Although the EXAFS spectra reflect an averaged structure including all solution Ca-species such as $Ca(BH_4)_2$, $CaBH_4^+$, and $Ca(BH_4)_3^-$, the veracity of the Ca–Ca correlation at ~4.44 Å and its consistency with DFT-predicted multimer structures are strong evidence for a significant population of multimeric species that are mediated by shared Ca–BH_4 interactions.

Additional experimental evidence for both Ca–BH_4 interactions and the tendency of $Ca(BH_4)_2$ to form multimers in THF is afforded by *ex situ* solvate crystal analysis. While these single crystals, formed by crystallization of concentrated $Ca(BH_4)_2$/THF, do not necessarily reflect the precise solvation structures present in solution, comparisons of crystal structures across a systematically varied set of solutions provide insight into relevant coordination structure trends, and this approach has been instructive for understanding Mg^{2+} electrolytes in a number of cases.[6] To this end, we have applied a combination of single crystal XRD and DFT to solve the previously unreported structure of THF_2-$Ca(BH_4)_2$, which crystallizes from the $Ca(BH_4)_2$/THF solution and matches the formula of the commercially available solvate solid (ESI, Table S3†). We find that this structure is polymeric with Ca^{2+} cations sharing coordination of axially arrayed BH_4^- anions and coordinated by radially arrayed THF molecules (Fig. 4a). Such a structure is indeed consistent with the proposed tendency of Ca^{2+} to prefer strong coordination with BH_4^- and its ability to form multimeric species in THF. In this case, a given BH_4^- coordinates through two hydrogens to one Ca^{2+} and through a third hydrogen to the opposing Ca^{2+} yielding intimate BH_4^-:Ca^{2+} interactions and minimizing the THF:Ca^{2+} CN. While the polymeric structure of $THF_2Ca(BH_4)_2$ is similar to that reported for the THF solvates of larger alkaline earth borohydrides, $THF_2Sr(BH_4)_2$ and $THF_2Ba(BH_4)_2$, it differs significantly from the reported monomeric structure of the smaller alkaline earth example, $THF_3Mg(BH_4)_2$.[14,54,55] In fact, the general absence of multimeric $Mg(BH_4)_2$ crystals from the greater body of literature across a variety of organic solvent systems has been considered noteworthy by previous authors and reflects a rather unique configurational attribute of the Mg^{2+} cation.[56] While dimeric Mg–Cl solvates in ethereal solvents are well-documented, *e.g.* $Mg_2Cl_3^+$ and $Mg_2Cl_2^{2+}$, the larger size of BH_4^- may induce additional strain in bridged solvate configurations that is not readily tolerated by the smaller and less configurationally flexible Mg^{2+} cation. Placing our Ca^{2+} results within the broader alkaline earth borohydride series (Mg^{2+}, Ca^{2+}, Sr^{2+}, Ba^{2+}) reveals that dications of lower charge density and therefore greater polarizability can stabilize multimeric BH_4^- complexes in THF, and that the critical transition in size-dependent behavior occurs between Mg^{2+} and Ca^{2+}.[14] This correlation between multimer formation tendency, ionicity, and electrochemical activity between $Ca(BH_4)_2$ and $Mg(BH_4)_2$, supports the hypothesized role of multimers in facilitating BH_4^- redistribution between ionic clusters.

Comparison of $Ca(BH_4)_2$ solvates produced from various ethereal solvents reveals that THF also plays a key role in stabilizing multimer formation. Replacement of THF by the more strongly coordinating, multidentate monoglyme (1,2-dimethoxyethane, G1) or diglyme (diethylene glycol dimethyl ether, G2) produces crystalline solvates with monomeric structures, consistent with previous reports (Fig. 4a).[57,58] $Sr(BH_4)_2$ also exhibits the same transition from polymeric to monomeric solvate structure upon replacement of THF by G2.[14] We find that the solubility of $Ca(BH_4)_2$ in these solvents is much less than in

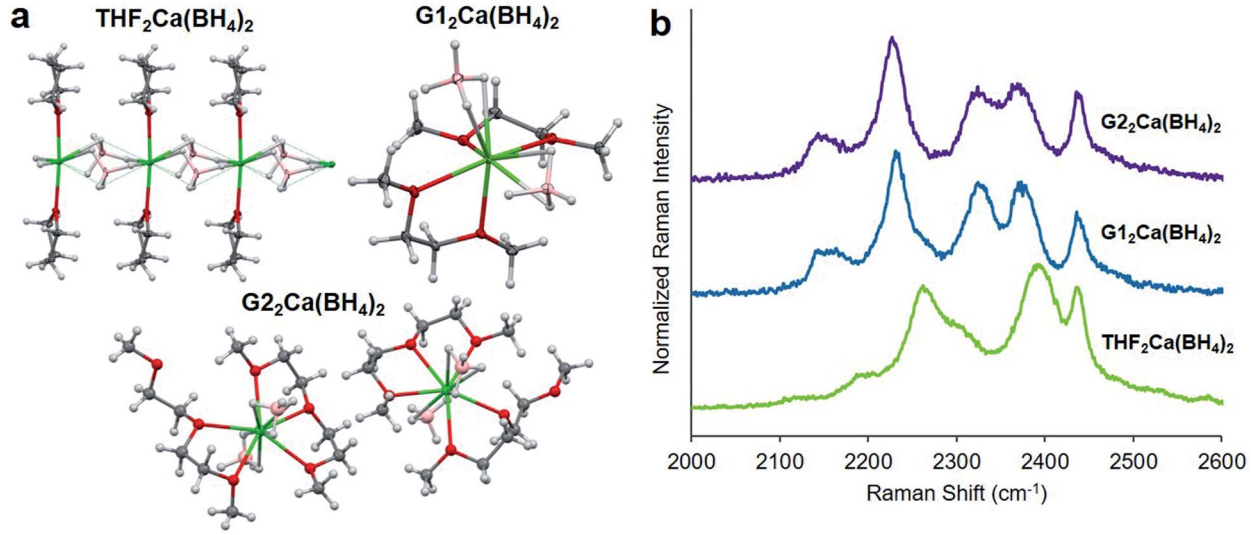

Fig. 4 (a) Solvate crystal structures determined through single crystal XRD. The G2 solvate structure comes from data generated in ref. 57 while the THF and G1 structures were determined in this work. (b) Raman ν(B–H) spectra for the indicated solvate crystals.

THF, as previously documented,[15] and this results in electrolytes that do not support reversible Ca electrodeposition (ESI, Fig. S10†). These results further strengthen the link between multimer formation and electrochemical activity in the $Ca(BH_4)_2$ system. The Raman ν(B–H) spectra of the glyme$_2$-$Ca(BH_4)_2$ solvates likewise exhibit distinctive line shapes relative to the THF solvate, highlighting the differences in BH_4^- coordination between multi- and monomeric structure (Fig. 4b). We note that the THF solvate spectra does not match that of the $Ca(BH_4)_2$/THF solution, indicating that the crystallized structure does not fully capture the distribution of solution Ca–BH_4 coordination structures. This is not surprising given that the solution structures either predicted by DFT or measured by EXAFS do not match the polymeric crystalline solvate in which Ca^{2+} is coordinated by only two THF molecules. Nevertheless, these solvent and cation driven changes in coordination and properties further highlight the importance of configurational flexibility as a driver for acceptable solubility, cation transport, and electrochemical stability in divalent BH_4^- electrolytes.

Configurational flexibility differences between $Ca(BH_4)_2$ and $Mg(BH_4)_2$ in THF are further demonstrated from analysis of the ν(B–H) region of the Raman vibrational spectrum. Comparison between the spectra of several borohydride salt solutions in THF highlights differences in the coordination structure tendencies of Ca^{2+} and Mg^{2+} (Fig. 5a). In a weakly interacting salt system, such as NBu_4BH_4, the spectrum is dominated by a relatively narrow set of bands near 2250 cm^{-1} corresponding to ionic BH_4^- for which the four B–H bonds are nominally equivalent because no specific cation–hydride bridging exists. Spectra of the metal borohydride salts ($LiBH_4$, $Mg(BH_4)_2$, $Ca(BH_4)_2$) are starkly different and reflect the complicated band splitting associated with covalently bound BH_4:M structures in which specific metal–hydride interactions distinguish coordinating or bridging (H_b) from non-coordinating or terminal (H_t) ligands.[56] Difficulties in deconvoluting the metal borohydride spectra while incorporating the free BH_4^- anion band leads to the conclusion that this species represents a very small fraction of the total borohydride inventory (ESI, Fig. S11†), consistent with our calculations and EXAFS results. Comparison of the spectral line shapes across the metal borohydride series further highlights the significant structural differences between $Mg(BH_4)_2$ and both $LiBH_4$ and $Ca(BH_4)_2$ in solution. While the two lower charge density cations (Li^+, Ca^{2+}) exhibit a similar set of several overlapping bands, the higher charge density Mg^{2+} cation exhibits two dominant and strongly separated bands suggestive of a more well-defined and static structural motif. These differences are further magnified by comparing the concentration dependence of the intensity normalized ν(B–H) spectral regions for the Mg^{2+} and Ca^{2+} salts in THF (Fig. 5b and c). While the normalized Raman spectra of BH_4:Mg^{2+} exhibit minimal change across the dilute to saturated concentration range, those of BH_4:Ca^{2+} exhibit a clear, progressive change in line shape. With increased concentration, the intensity of the 2324 cm^{-1} band is reduced relative to that of the other bands, while the band at 2230 cm^{-1} exhibits an increase in relative intensity. These spectral changes indicate that borohydride coordination is altered with increased concentration; changes that we ascribe to formation of $Ca_2(BH_4)_4$ and subsequently $CaBH_4^+$ and $Ca(BH_4)_3^-$ at significant concentrations relative to the parent monomer, $Ca(BH_4)_2$. Attempts to explicitly interpret the measured spectral changes based on simulated Raman spectra of these clusters were inconclusive, owing to the complexity of the coordinated BH_4^- vibrational modes. However, measurements of THF coordination changes within the ν(C–O)/ν(C–C) region over these concentration ranges are less ambiguous and suggest that the THF:Ca^{2+} CN decreases at high concentrations while the THF:Mg^{2+} CN does not (ESI, Fig. S12†). Such differences are consistent with the increase in relative BH_4^-:Ca^{2+} interactions expected for multimeric species in $Ca(BH_4)_2$/THF and with the absence of such multimeric interactions in $Mg(BH_4)_2$/THF. Hence, based on the ionicity trends, DFT cluster

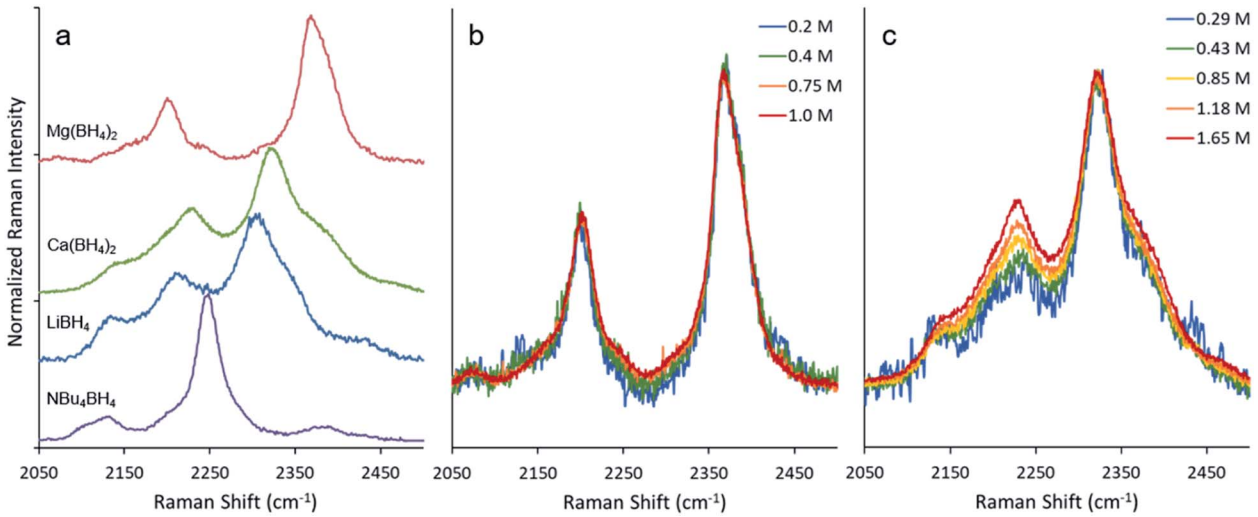

Fig. 5 (a) Plots of the Raman ν(B–H) spectral region for representative examples of several borohydride salt solutions in THF. (b and c) Raman spectra of the ν(B–H) region for $Mg(BH_4)_2$/THF (b) and $Ca(BH_4)_2$/THF (c) as a function of concentration.

energetics, EXAFS, and solvate XRD, we contend that the $Ca(BH_4)_2$/THF solution evolves from a population of mostly neutral monomers at low concentration to one consisting of dimers and associated ionic clusters ($CaBH_4^+$ and $Ca(BH_4)_3^-$) at high concentrations, as enabled by the configurational flexibility of Ca^{2+} relative to Mg^{2+}. We expect these configurational differences to have important ramifications for future comparisons between Ca^{2+} and Mg^{2+} electrolytes.

Conclusions

In this work we have documented the surprising importance of ion association and multimer formation in supporting high electrochemical rate and reversibility of Ca metal deposition in high concentration $Ca(BH_4)_2$/THF electrolytes. The proposed ion formation pathway hinges on the greater configurational flexibility of Ca^{2+} relative to Mg^{2+}, addressing the more general themes of coordination tendencies in divalent electrolytes. These integrated experimental and computational results show that increasing salt concentration and decreasing cation charge density (*i.e.* from Mg^{2+} to Ca^{2+}) guides solution speciation from uncharged neutral species toward multimers and ionic clusters capable of delivering Ca^{2+} at appreciable rates while sparing parasitic loss from electrolyte decomposition. This combination of electrolyte attributes facilitates the achievement of CE's over 97% and motivates further scientific exploration into the nature and control of solvation interactions in divalent metal chemistries, particularly those occurring under extremely reducing conditions.

Conflicts of interest

There are no conflicts of interest to declare.

Acknowledgements

This work was supported by the Joint Center for Energy Storage Research, an Energy Innovation Hub funded by the U.S. Department of Energy. Sandia National Laboratories is a multimission laboratory managed and operated by National Technology & Engineering Solutions of Sandia, LLC, a wholly owned subsidiary of Honeywell International Inc., for the U.S. Department of Energy's National Nuclear Security Administration under contract DE-NA0003525. This research used resources of the National Energy Research Scientific Computing Center, a DOE Office of Science User Facility supported by the Office of Science of the U.S. Department of Energy under contract no. DE-AC02-05CH11231. This research used resources of the Advanced Photon Source, an Office of Science User Facility operated for the U.S. Department of Energy (DOE) Office of Science by Argonne National Laboratory and was supported by the U.S. DOE under Contract No. DE-AC02-06CH11357. The authors thank G. E. Sterbinsky for his help at beamline 9-BM in the setup and analysis of the XAS data. This paper describes objective technical results and analysis. Any subjective views or opinions that might be expressed in the paper do not necessarily represent the views of the U.S. Department of Energy or the United States Government.

References

1 C. B. Bucur, T. Gregory, A. G. Oliver and J. Muldoon, *J. Phys. Chem. Lett.*, 2015, **6**, 3578–3591.
2 D. Aurbach, R. Skaletsky and Y. Gofer, *J. Electrochem. Soc.*, 1991, **138**, 3536–3545.
3 O. Mizrahi, N. Amir, E. Pollak, O. Chusid, V. Marks, H. Gottlieb, L. Larush, E. Zinigrad and D. Aurbach, *J. Electrochem. Soc.*, 2008, **155**, A103–A109.
4 C. Liao, B. Guo, D.-e. Jiang, R. Custelcean, S. M. Mahurin, X.-G. Sun and S. Dai, *J. Mater. Chem. A*, 2014, **2**, 581–584.
5 R. Mohtadi, M. Matsui, T. S. Arthur and S.-J. Hwang, *Angew. Chem., Int. Ed.*, 2012, **51**, 9780–9783.
6 O. Tutusaus, R. Mohtadi, T. S. Arthur, F. Mizuno, E. G. Nelson and Y. V. Sevryugina, *Angew. Chem., Int. Ed.*, 2015, **54**, 7900–7904.

7 I. Shterenberg, M. Salama, H. D. Yoo, Y. Gofer, J. B. Park, Y. K. Sun and D. Aurbach, *J. Electrochem. Soc.*, 2015, **162**, A7118–A7128.
8 A. Ponrouch, C. Frontera, F. Bardé and M. R. Palacín, *Nat. Mater.*, 2015, **15**, 169.
9 A. L. Lipson, S. Kim, B. Pan, C. Liao, T. T. Fister and B. J. Ingram, *J. Power Sources*, 2017, **369**, 133–137.
10 M. Cabello, F. Nacimiento, J. R. González, G. Ortiz, R. Alcántara, P. Lavela, C. Pérez-Vicente and J. L. Tirado, *Electrochem. Commun.*, 2016, **67**, 59–64.
11 D. Wang, X. Gao, Y. Chen, L. Jin, C. Kuss and P. G. Bruce, *Nat. Mater.*, 2017, **17**, 16.
12 Z. Y. Li, O. Fuhr, M. Fichtner and Z. Zhao-Karger, *Energy Environ. Sci.*, 2019, **12**, 3496–3501.
13 A. Shyamsunder, L. E. Blanc, A. Assoud and L. F. Nazar, *ACS Energy Lett.*, 2019, **4**, 6.
14 M. Bremer, H. Nöth, M. Thomann and M. Schmidt, *Chem. Ber.*, 1995, **128**, 455–460.
15 H. Hagemann and R. Černý, *Dalton Trans.*, 2010, **39**, 6006–6012.
16 V. D. Makhaev, *Russ. Chem. Rev.*, 2000, **69**, 795–816.
17 K. Ta, R. Zhang, M. Shin, R. T. Rooney, E. K. Neumann and A. A. Gewirth, *ACS Appl. Mater. Interfaces*, 2019, **11**, 21536–21542.
18 J. D. Deetz, F. Cao, Q. Wang and H. Sun, *J. Electrochem. Soc.*, 2018, **165**, A61–A70.
19 J. D. Deetz, F. Cao and H. Sun, *J. Electrochem. Soc.*, 2018, **165**, A2451–A2457.
20 D. Samuel, C. Steinhauser, J. G. Smith, A. Kaufman, M. D. Radin, J. Naruse, H. Hiramatsu and D. J. Siegel, *ACS Appl. Mater. Interfaces*, 2017, **9**, 43755–43766.
21 Y. Shao, T. Liu, G. Li, M. Gu, Z. Nie, M. Engelhard, J. Xiao, D. Lv, C. Wang, J.-G. Zhang and J. Liu, *Sci. Rep.*, 2013, **3**, 3130.
22 A. K. Katz, J. P. Glusker, S. A. Beebe and C. W. Bock, *J. Am. Chem. Soc.*, 1996, **118**, 5752–5763.
23 E. Carafoli and J. Krebs, *J. Biol. Chem.*, 2016, **291**, 20849–20857.
24 B. Ravel and M. Newville, *J. Synchrotron Radiat.*, 2005, **12**, 537–541.
25 J. J. Rehr and R. C. Albers, *Rev. Mod. Phys.*, 2000, **72**, 621–654.
26 M. J. Abraham, T. Murtola, R. Schulz, S. Páll, J. C. Smith, B. Hess and E. Lindahl, *SoftwareX*, 2015, **1–2**, 19–25.
27 L. Martínez, R. Andrade, E. G. Birgin and J. M. Martínez, *J. Comput. Chem.*, 2009, **30**, 2157–2164.
28 C. Caleman, P. J. van Maaren, M. Hong, J. S. Hub, L. T. Costa and D. van der Spoel, *J. Chem. Theory Comput.*, 2012, **8**, 61–74.
29 W. L. Jorgensen, D. S. Maxwell and J. Tirado-Rives, *J. Am. Chem. Soc.*, 1996, **118**, 11225–11236.
30 G. A. Kaminski, R. A. Friesner, J. Tirado-Rives and W. L. Jorgensen, *J. Phys. Chem. B*, 2001, **105**, 6474–6487.
31 N. N. Rajput, X. Qu, N. Sa, A. K. Burrell and K. A. Persson, *J. Am. Chem. Soc.*, 2015, **137**, 3411–3420.
32 J. Self, B. M. Wood, N. N. Rajput and K. A. Persson, *J. Phys. Chem. C*, 2018, **122**, 1990–1994.
33 M. J. Frisch, G. W. Trucks, H. B. Schlegel, G. E. Scuseria, M. A. Robb, J. R. Cheeseman, G. Scalmani, V. Barone, G. A. Petersson and H. Nakatsuji, *Gaussian 16 Rev. B.01 Release Notes*, Wallingford, CT, 2016.
34 Y. Zhao and D. G. Truhlar, *Theor. Chem. Acc.*, 2008, **120**, 215–241.
35 D. Rappoport and F. Furche, *J. Chem. Phys.*, 2010, **133**, 134105.
36 Z. Zhao-Karger, R. Liu, W. Dai, Z. Li, T. Diemant, B. P. Vinayan, C. Bonatto Minella, X. Yu, A. Manthiram, R. J. Behm, M. Ruben and M. Fichtner, *ACS Energy Lett.*, 2018, **3**, 2005–2013.
37 J. T. Herb, C. A. Nist-Lund and C. B. Arnold, *ACS Energy Lett.*, 2016, **1**, 1227–1232.
38 S. G. McArthur, R. Jay, L. Geng, J. Guo and V. Lavallo, *Chem. Commun.*, 2017, **53**, 4453–4456.
39 E. C. Ashby, F. R. Dobbs and H. P. Hopkins, *J. Am. Chem. Soc.*, 1973, **95**, 2823–2829.
40 H. Farber and S. Petrucci, *J. Phys. Chem.*, 1976, **80**, 327–335.
41 M. Delsignore, H. Farber and S. Petrucci, *J. Phys. Chem.*, 1985, **89**, 4968–4973.
42 S. Petrucci, M. C. Masiker and E. M. Eyring, *J. Solution Chem.*, 2008, **37**, 1031–1035.
43 R. M. Fuoss and C. A. Kraus, *J. Am. Chem. Soc.*, 1933, **55**, 2387–2399.
44 J. Self, N. T. Hahn, K. D. Fong, S. A. McClary, K. R. Zavadil and K. A. Persson, *J. Phys. Chem. Lett.*, 2020, **11**, 2046–2052.
45 L. Doucey, M. Revault, A. Lautié, A. Chaussé and R. Messina, *Electrochim. Acta*, 1999, **44**, 2371–2377.
46 H. Farber and S. Petrucci, *J. Phys. Chem.*, 1975, **79**, 1221–1227.
47 P. Eberspächer, E. Wismeth, R. Buchner and J. Barthel, *J. Mol. Liq.*, 2006, **129**, 3–12.
48 L. F. Wan, B. R. Perdue, C. A. Apblett and D. Prendergast, *Chem. Mater.*, 2015, **27**, 5932–5940.
49 A. Benmayza, M. Ramanathan, T. S. Arthur, M. Matsui, F. Mizuno, J. Guo, P.-A. Glans and J. Prakash, *J. Phys. Chem. C*, 2013, **117**, 26881–26888.
50 Y. Viestfrid, M. D. Levi, Y. Gofer and D. Aurbach, *J. Electroanal. Chem.*, 2005, **576**, 183–195.
51 C. J. Barile, E. C. Barile, K. R. Zavadil, R. G. Nuzzo and A. A. Gewirth, *J. Phys. Chem. C*, 2014, **118**, 27623–27630.
52 P. Canepa, S. Jayaraman, L. Cheng, N. N. Rajput, W. D. Richards, G. S. Gautam, L. A. Curtiss, K. A. Persson and G. Ceder, *Energy Environ. Sci.*, 2015, **8**, 3718–3730.
53 T. S. Arthur, P.-A. Glans, N. Singh, O. Tutusaus, K. Nie, Y.-S. Liu, F. Mizuno, J. Guo, D. H. Alsem, N. J. Salmon and R. Mohtadi, *Chem. Mater.*, 2017, **29**, 7183–7188.
54 E. B. Lobkovskii, L. V. Titov, M. D. Levicheva and A. N. Chekhlov, *J. Struct. Chem.*, 1990, **31**, 506–508.
55 E. B. Lobkovskii, L. V. Titov, S. B. Psikha, M. Y. Antipin and Y. T. Struchkov, *J. Struct. Chem.*, 1983, **23**, 644–646.
56 M. Bremer, H. Nöth and M. Warchhold, *Eur. J. Inorg. Chem.*, 2003, **2003**, 111–119.
57 E. B. Lobkovskii, A. N. Chekhlov, M. D. Levicheva and L. V. Titov, *Soviet Journal of Coordination Chemistry*, 1988, **14**, 543–550.
58 E. Hanecker, J. Moll and H. Noth, *Z. Naturforsch. B Chem. Sci.*, 1984, **39**, 424–430.

